Atmos. Chem. Phys., 13, 12433–12450, 2013
www.atmos-chem-phys.net/13/12433/2013/
doi:10.5194/acp-13-12433-2013

Atmospheric Chemistry and Physics Open Access

Anthropogenic agent implicated as a prime driver of shift in precipitation in eastern China in the late 1970s

T. Wang[1], H. J. Wang[1,2,*], O. H. Otterå[3,6], Y. Q. Gao[1,4,6], L. L. Suo[4,6], T. Furevik[5,6], and L. Yu[5,6]

[1]Nansen-Zhu International Research Center, Institute of Atmospheric Physics, Chinese Academy of Sciences, Beijing 100029, China
[2]Climate Change Research Center, Chinese Academy of Sciences, Beijing 100029, China
[3]Uni Climate, Uni Research, Bergen, Norway
[4]Nansen Environmental and Remote Sensing Center, Bergen, Norway
[5]Geophysical Institute, University of Bergen, Bergen, Norway
[6]Bjerknes Centre for Climate Research, Bergen, Norway
[*]now at: Nansen-Zhu International Research Center, Institute of Atmospheric Physics, Chinese Academy of Sciences, Beijing 100029, China

Correspondence to: H. J. Wang (wanghj@mail.iap.ac.cn)

Received: 20 January 2013 – Published in Atmos. Chem. Phys. Discuss.: 7 May 2013
Revised: 13 November 2013 – Accepted: 21 November 2013 – Published: 19 December 2013

Abstract. Observation shows that eastern China experienced an interdecadal shift in the summer precipitation during the second half of the 20th century. The summer precipitation increased in the middle and lower reaches of the Yangtze River valley, whereas it decreased in northern China. Here we use a coupled ocean–atmosphere general circulation model and multi-ensemble simulations to show that the interdecadal shift is mainly caused by the anthropogenic forcing. The rapidly increasing greenhouse gases induce a notable Indian Ocean warming, causing a westward shift of the western Pacific subtropical high (WPSH) and a southward displacement of the East Asia westerly jet (EAJ) on an interdecadal timescale, leading to more precipitation in Yangtze River valley. At the same time the surface cooling effects from the stronger convection, higher precipitation and rapidly increasing anthropogenic aerosols contribute to a reduced summer land–sea thermal contrast. Due to the changes in the WPSH, the EAJ and the land–sea thermal contrast, the East Asian summer monsoon weakened resulting in drought in northern China. Consequently, an anomalous precipitation pattern started to emerge over eastern China in the late 1970s. According to the model, the natural forcing played an opposite role in regulating the changes in WPSH and EAJ, and postponed the anthropogenically forced climate changes in eastern China. The Indian Ocean sea surface temperature is crucial to the response, and acts as a bridge to link the external forcings and East Asian summer climate together on a decadal and longer timescales. Our results further highlight the dominant roles of anthropogenic forcing agents in shaping interdecadal changes of the East Asian climate during the second half of the 20th century.

1 Introduction

The East Asian summer monsoon (EASM) leads to heavy rainfall in June, July and August along thousands of kilometers of rain belts affecting the East Asian countries, encompassing one third of the world's population. In fact, EASM contributes as much as 40–50 % (60–70 %) of the annual precipitation in southern China (northern China) (Ding, 1992; Gong and Ho, 2003). Observations show that the EASM has experienced a significant weakening during the second half of the 20th century (H. J. Wang, 2001, 2002). This noticeable weakening concurred with more summer rainfall in the middle and lower reaches of the Yangtze River valley (YRV) and less rainfall in northern China (Gong and Ho, 2002; Zhai et al., 2005). This interdecadal variation of the summer precipitation (IVSP) has been referred to as the southern flood and northern drought pattern (Ding et al., 2008, 2009; Zhao et al.,

2010). The weakening of the EASM and the associated IVSP have large impacts on agriculture, water resources and society for nearly 1 billion people, in particular in eastern China with a dense population and concentrated industries and agricultures (Piao et al., 2010). Despite the critical importance of the weakened EASM and the IVSP for China, the ultimate causes for this interdecadal shift remain unclear (Ding et al., 2009; Bollasina et al., 2011; Zuo et al., 2012).

Both natural (e.g., volcanoes) and anthropogenic (greenhouse gases and tropospheric aerosols) factors can affect the global and regional climate. For instance, a significant global reduction in precipitation over land following the Mount Pinatubo eruption in 1991 has been documented (Trenberth and Dai, 2007). Evidence from paleo-proxy reconstructions also suggests a link between volcanic eruptions and decreased summer precipitation in China over the past five centuries (Shen et al., 2008). A recent study suggested that volcanic eruptions can impact the Pacific Decadal Oscillation (PDO) (T. Wang et al., 2012), which is a key factor affecting global and regional climate on a decadal timescale (Mantua and Hare, 2002; H. Wang et al., 2007; Zhu et al., 2011). The rapidly increasing concentrations of atmospheric greenhouse gases also have strong impacts on the climate. According to the Fourth Assessment Report of the IPCC (IPCC AR4), most of the observed increase in global average temperature since the mid-20th century is very likely due to the increase in greenhouse gas concentrations (Hegerl et al., 2007). It is also well known that the increase in tropospheric aerosols during the same period has produced a substantial cooling, particularly over land, and that this cooling could have reduced greenhouse-gas-induced warming by as much as 50 % during the 20th century (Huber and Knutti, 2012). Additionally, high tropospheric aerosol concentrations can slow down the tropical meridional overturning circulation and decrease regional summer precipitation in South Asia (Bollasina et al., 2011).

The reasons for the weakening of the EASM and the accompanying IVSP in eastern China are still not fully understood due to the complex nature of the EASM system (e.g., land–sea thermal contrast, western Pacific subtropical high, topography) and the mixture of diverse forcing agents (Ding and Chan, 2005). It is difficult for observational studies alone to address all these issues fully. Therefore, the combination of in situ data, atmosphere reanalysis data and modeling studies becomes essential in order to understand the causes and governing mechanisms behind the weakening of the EASM. However, the IPCC AR4 models and other ensemble simulations have so far generally failed to reproduce the observed IVSP in eastern China during the late 20th century (Jiang and Wang, 2005; Meehl et al., 2008; Bollasina et al., 2011). Therefore, it is still under debate to what extent the recently observed IVSP in eastern China is caused by natural climate variability, human activities, or both.

In this study, we assess the relative roles of anthropogenic forcings and natural forcings in forming the IVSP using multi-ensemble simulations driven by different combinations of forcing agents. In Sect. 2 we describe the model and experiment design, whereas the observational and simulated interdecadal climate changes in eastern China are investigated in Sect. 3. The paper is concluded with a summary and a discussion in Sect. 4.

2 Model, experimental design and data

2.1 Model

The climate model used in this study is an updated version of the Bergen Climate Model (BCM) (Furevik et al., 2003), a global, coupled atmosphere–ocean–sea-ice general circulation model (GCM). The atmosphere component is the spectral atmospheric GCM ARPEGE (Déqué et al., 1994). In this study, ARPEGE is run with a truncation at wave number 63 (T_L63), and a time step of 1800 s. A total of 31 vertical levels are employed, ranging from the surface to 10 hPa. The physical parametrization is divided into several explicit schemes, each calculating the flux of mass, energy and/or momentum due to a specific physical process (Furevik et al., 2003). The ocean component is MICOM (Bleck and Smith, 1990; Bleck et al., 1992), a global isopycnic coordinate ocean GCM. With the exception of the equatorial region, the ocean grid is almost regular with a horizontal grid spacing of approximately $2.4^\circ \times 2.4^\circ$. In order to resolve the dynamics near the Equator better, the horizontal spacing in the meridional direction is gradually decreased to 0.8° along the Equator. The model has a stack of 34 isopycnic layers in the vertical, with potential densities ranging from 1029.514 to 1037.800 $\mathrm{kg\,m^{-3}}$, and a non-isopycnic surface mixed layer on top providing the linkage between the atmospheric forcing and the ocean interior. The sea-ice model is GELATO, a dynamic–thermodynamic sea-ice model that includes multiple ice categories (Salas-Melia, 2002). The OASIS (version 2) coupler (Terray and Thual, 1995; Terray et al., 1995) has been used to couple the atmosphere and ocean models.

The model is run without any flux adjustments. The preindustrial control simulation reproduces the major features of the global climate, and is stable for several centuries (Otterå et al., 2009).

2.2 Experimental design

The external forcings used in this study include the natural forcings (total solar irradiance and volcanoes) and the anthropogenic forcings (well-mixed greenhouse gases and tropospheric sulfate aerosols). The total solar irradiance forcing (Fig. 1) (Crowley et al., 2003) is incorporated as variations in the effective solar constant in the BCM. This modifies the top of the atmosphere shortwave flux in the BCM. The volcanic aerosol forcing (Fig. 1) (Crowley et al., 2003) includes the monthly optical depths at 0.55 µm in the middle of the visible spectrum in four bands (90–30° N, 30° N–Equator,

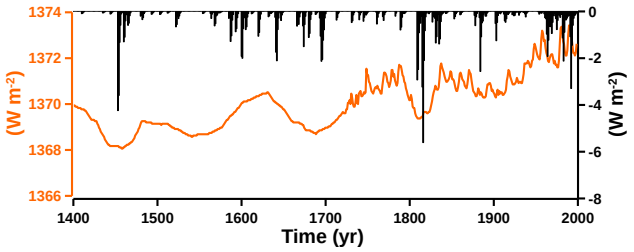

Fig. 1. Volcanic forcing (black shading) and total solar irradiance forcing (orange line) for the past 600 yr.

Equator–30° S and 30–90° S). The aerosol loading was distributed in each stratospheric model level using a weighting function (Otterå, 2008). The volcanic mass of the stratospheric aerosols was then calculated at each grid point and model level in the stratosphere by dividing the total aerosol concentration by the total air mass of all stratospheric levels at that grid point. The tropospheric sulfate aerosol forcing fields (Fig. 2) are based on the simulation of the historical sulfur cycle as prepared for the IPCC AR4 (Lefohn et al., 1999; Boucher and Pham, 2002). In the current version of BCM, only the direct effect and first indirect effect of tropospheric sulfate aerosol have been included. The horizontal distribution of the other troposphere aerosol species are held constant at their default values, which are defined according to Tanre et al. (1984). The changes in the well-mixed greenhouse gases are taken from the forcing data set prepared for the EU project ENSEMBLES (Fig. 3) (Johns et al., 2011). This forcing data set includes the annual concentrations of the five most important trace gases (i.e., CO_2, CH_4, N_2O, CFC-11 and CFC-12) for the period 1850–1999 (http://www.cnrm.meteo.fr/ensembles/public/results/results.html).

Here, we use ensemble model simulations to investigate the relative importance of anthropogenic and natural forcing factors to the recent shift in precipitation and associated climate changes in eastern China. Four sets of historical simulations covering the period from 1850 to 1999 were carried out: (i) ALL150, a five-member ensemble with changes in both natural forcing agents (solar variations and volcanoes) and anthropogenic forcing agents (well-mixed greenhouse gases and tropospheric sulfate aerosols) included; (ii) ANT150, a five-member ensemble with the anthropogenic forcing agents only; (iii) NAT150, a five-member ensemble with the natural forcing agents only; and (iv) CTL150, a five-member ensemble with no year-to-year variations in the external forcing agents and with greenhouse gas and tropospheric sulfate aerosol concentration fixed at pre-industrial (1850) levels. Since the focus of this study has been to address the causes of the observed IVSP in eastern China during the late 20th century, we have restricted our model analysis to the period 1958 to 1995 (whereas the whole simulation for CTL150).

The initial conditions for ALL150, ANT150 and NAT150 were taken from a 600 yr historical simulation forced by natural variations (Otterå et al., 2010). The initial conditions for CTL150 were taken from a 600 yr pre-industrial control run (Otterå et al., 2009). Each experiment consists of five ensemble members, where each member was initialized using the common method of taking different atmosphere, but identical ocean, start conditions for the model (Collins et al., 2006). Due to the highly chaotic nature of the atmospheric model, each realization is statistically independent after only a few weeks of integration. In our case, the different atmospheric initial conditions for these four sets of simulations were generated from a previous 20-day simulation using a daily restart file every 5 days. This perturbation methodology is in no way optimal in terms of, for example, sampling the likely range of subdecadal atmosphere–ocean analysis error. However, it is sufficient to generate ensemble spread on the timescales of interest here.

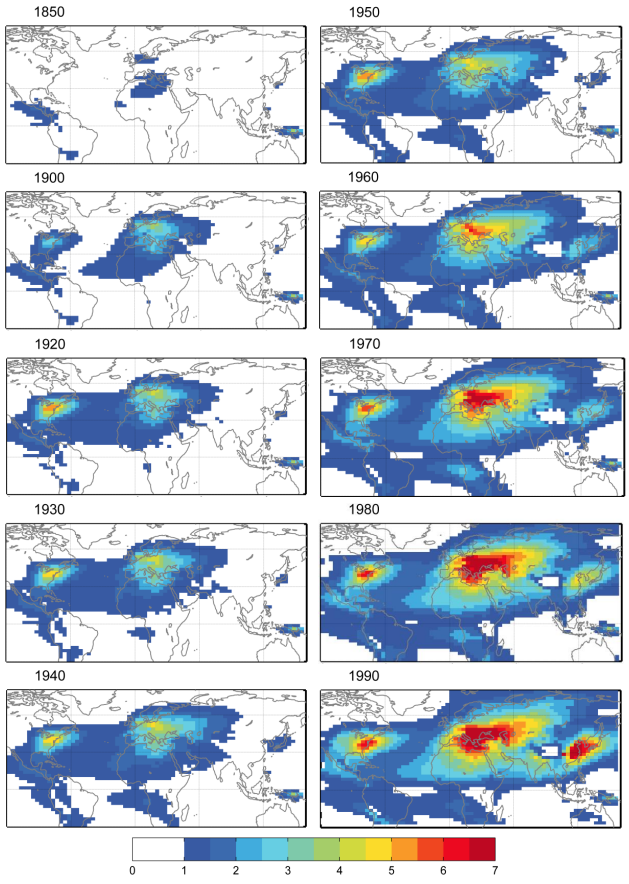

Fig. 2. Annual mean tropospheric sulfate aerosol burden (mg S m^{-2}) for the years 1850, 1900, 1920, 1930, 1940, 1950, 1960, 1970, 1980 and 1990.

2.3 Data

In this study, two sets of observed precipitation and surface air temperature were analyzed. One is the observed data from 740 meteorological stations (STN) collected by the China

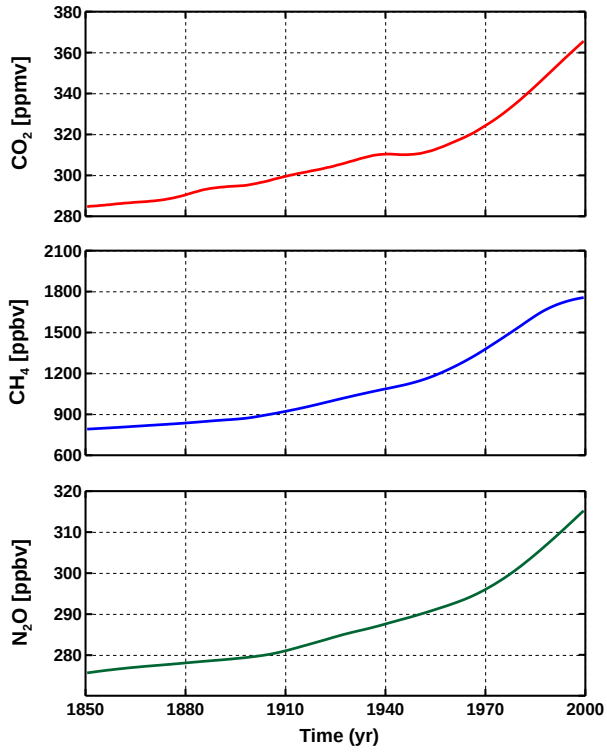

Fig. 3. Annual concentrations of three most important well-mixed greenhouse gases used to force the model for the period of 1850–1999.

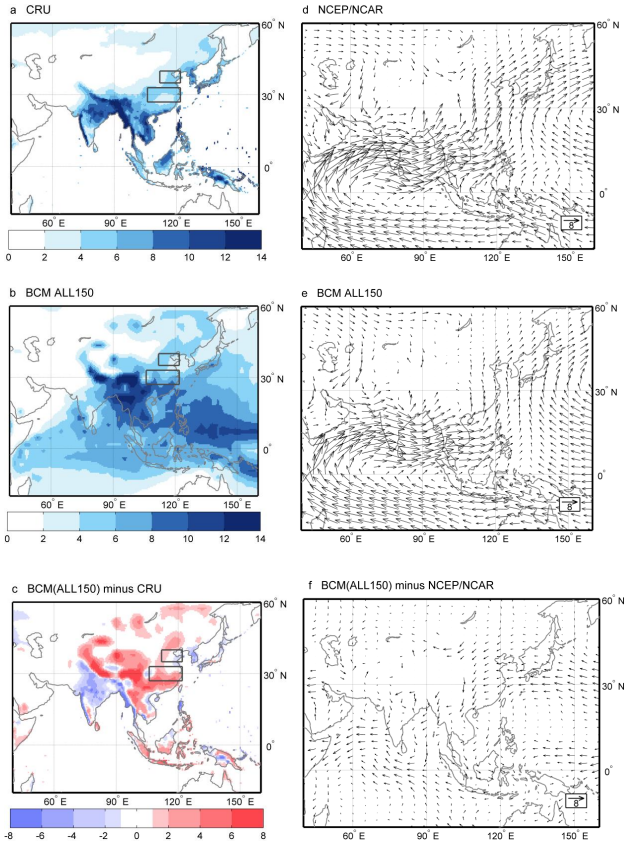

Fig. 4. Summer precipitation (June-July-August, unit: mm day^{-1}) for the period of 1958–1995 from **(a)** CRU data set, **(b)** BCM ALL150, and **(c)** BCM (ALL150) minus CRU data set. Summer 850 hPa wind field (unit: m s^{-1}) for the same period from **(d)** NCEP/NCAR reanalysis data set, **(e)** BCM ALL150, and **(f)** BCM (ALL150) minus NCEP/NCAR. Regions with elevations higher than 1500 m are blank. The boxes denote the analysis drought region in North China (NC, 35–40° N, 112–122° E) and flood region in Yangtze River valley (YRV, 27–33° N, 106–122° E), over which the average precipitation trends are calculated.

Meteorological Administration (CMA); the other is the Climate Research Unit (CRU) data set (Mitchell and Jones, 2005). In addition, the observed data from the Hadley Centre Sea Level Pressure data set (HadSLP2) (Allan and Ansell, 2006), the Hadley Centre monthly Sea Surface Temperature data set (HadISST) (Rayner et al., 2003), the Extended Reconstructed Sea Surface Temperature data set (ERSST, version v3b) (Smith et al., 2008), the National Centers for Environmental Prediction/National Center for Atmospheric Research (NCEP/NCAR) reanalysis data (Kalnay et al., 1996), and the European Centre for Medium-range Weather Forecast (ECMWF) 40 yr Reanalysis (ERA-40) (Uppala et al., 2005) were also used to evaluate model performance and to investigate interdecadal climate changes over eastern China during the second half of the 20th century.

For the statistical analyses, significance levels were calculated using a standard t test in this study. The Mann–Kendall test (Mann, 1945) was used to estimate the statistical significance of the linear trends. The Pearson's linear correlation coefficient was used to describe the significance of the correlation coefficients between the data and model.

3 Results

3.1 Evaluation of the model's climatology

We first examine whether BCM can reproduce observed East Asian summer climatology. Figure 4 shows that the BCM ALL150 ensemble can simulate the large-scale summer precipitation and wind fields at 850 hPa reasonably well for the period of 1958–1995. There are positive precipitation biases over South China and West China in the BCM, but model biases are small over eastern China, which is our region of interest. Overall, the model is able to reproduce the spatial pattern of East Asian summer climate fairly realistically and should therefore constitute a good starting point to address the weakened EASM and the IVSP in eastern China.

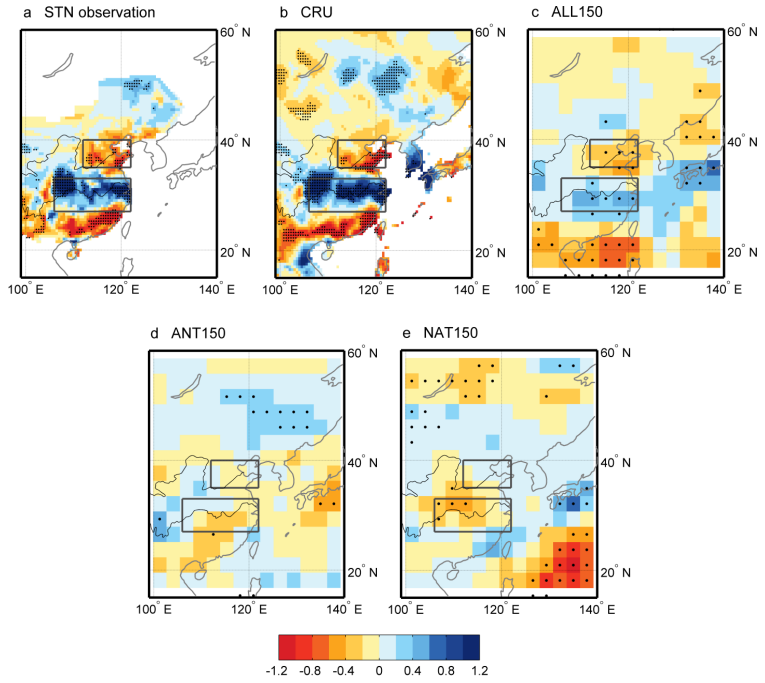

Fig. 5. The differences (1978–1995 minus 1958–1977) in summer precipitation (June-July-August, unit: mm d^{-1}) in the **(a)** STN data, **(b)** CRU data set, **(c)** ALL150, **(d)** ANT150, and **(e)** NAT150. Areas with confidence level exceeding 90 % are denoted with dots.

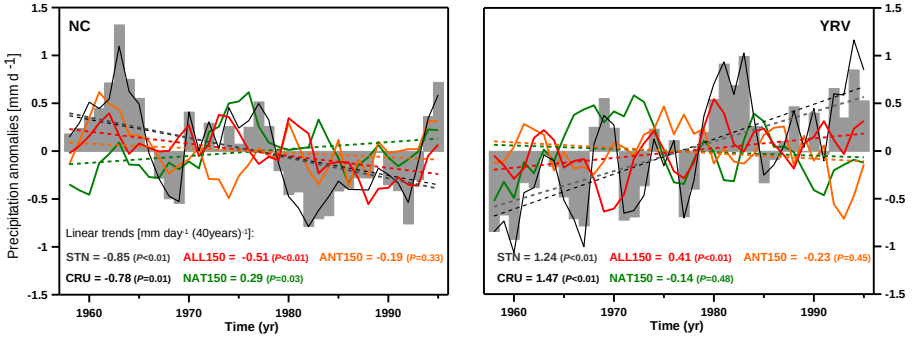

Fig. 6. Time series of 3 yr running mean summer precipitation anomalies (June-July-August, unit: mm d^{-1}) over the NC and YRV regions (see the black boxes in Fig. 5). Anomalies are calculated as deviations from the 1958–1995 climatology. The gray histograms and black lines are based on the STN and CRU TS 3.0 observational data sets, respectively. The red, orange, and green lines are for the ALL150, ANT150, and NAT150 historical integrations, respectively. The least-squares linear trends during 1958–1995 are plotted as dashed lines in the respective colors.

3.2 The observational and simulated changes in summer precipitation

It can be seen that the precipitation increases significantly over the middle and lower reaches of the YRV, whereas it decreases over the North China (NC) and along the coasts of South China from the period 1958–1977 to the period 1978–1995 (Fig. 5). The simulated precipitation pattern in ALL150 qualitatively matches the observed anomalous precipitation pattern, but the magnitude of the precipitation anomaly in the model is less than those in the STN and CRU data sets. ALL150 also reproduces realistic precipitation anomalies in most other regions of China and adjacent areas. In contrast, neither the ANT150 nor NAT150 is able to capture the observed changes in summer precipitation over eastern China. In ANT150, positive precipitation anomalies can be observed over northeast China. There are no significant precipitation anomalies over the NC and YRV. In NAT150, negative precipitation anomalies appear over central China and the northern parts of East Asia continent, which are opposite to the observation.

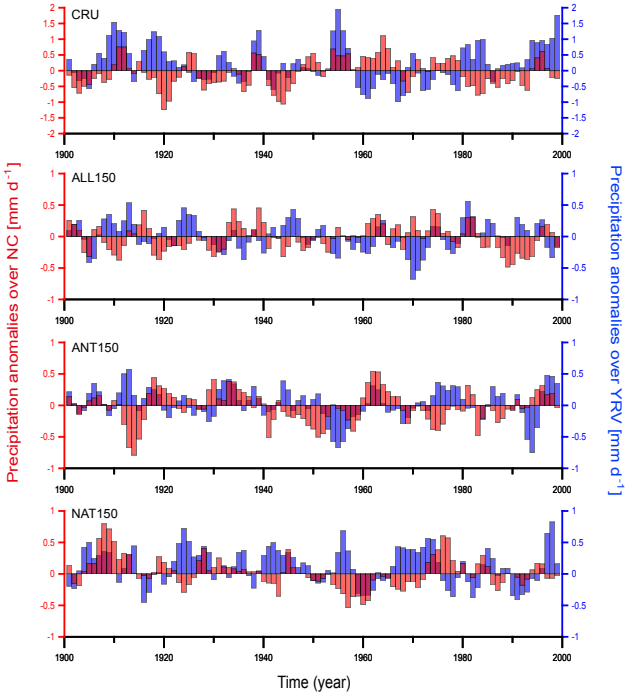

Fig. 7. Time series of summer precipitation anomalies (June-July-August, unit: mm d^{-1}) over the NC and YRV regions during the whole 20th century (see the black boxes in Fig. 5). Anomalies are calculated as deviations from the 1958–1995 climatology. The red and blue histograms are for the NC and YRV, respectively. A first-order Butterworth filter has been used to low-pass-filter (7 yr) all the time series to highlight precipitation anomalies on decadal timescales.

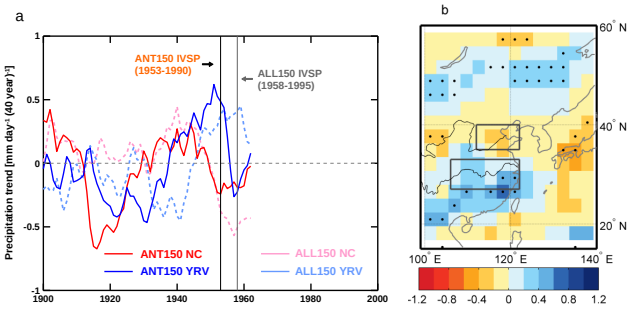

Fig. 8. (a) Running interdecadal trends for the summer precipitation anomalies over the NC and YRV regions for ALL150 and ANT150. The running window width is 38 yr, same length as the period of 1958–1995 (i.e., the value in the year 1958 represents the linear trend for the period of 1958–1995). **(b)** ANT150 simulated differences (1973–1990 minus 1953–1972) in summer (June-July-August) precipitation (unit: mm d^{-1}). Areas with confidence level exceeding 90 % are denoted with dots.

The time evolution of observed summer precipitation shows an interdecadal shift at the end of the 1970s, with drier conditions in the NC (35–40° N, 112–122° E) and wetter conditions in the YRV (27–33° N, 106–122° E, boxes in Figs. 4 and 5) for the latter two decades (Fig. 6). The STN data show linear trends of $-0.85\,\mathrm{mm\,day^{-1}}\ (40\,\mathrm{yr})^{-1}$ for the NC and $1.24\,\mathrm{mm\,day^{-1}}\ (40\,\mathrm{yr})^{-1}$ for the YRV, which are both statistically significant at the 99 % confidence level ($P < 0.01$). Comparable trends are also seen in the CRU data set.

The ALL150 captures the interdecadal changes in the precipitation over eastern China, although linear trends are weaker: $-0.51\,\mathrm{mm\,day^{-1}}\ (40\,\mathrm{yr})^{-1}$ ($P < 0.01$) and $0.41\,\mathrm{mm\,day^{-1}}\ (40\,\mathrm{yr})^{-1}$ ($P < 0.01$) for the NC and YRV, respectively. The other individual ensembles fail to capture the observed trend. Particularly in NAT150, the precipitation trends for the NC and YRV regions are actually reversed compared to the observations. The results thus indicate that the IVSP in the late 1970s is likely caused by the external forcings including both anthropogenic and natural factors.

Furthermore, we examined the longer time evolution of summer precipitation over these two regions focusing on a decadal timescale (Fig. 7). It is found that a similar IVSP occurs at the beginning of the 1970s in ANT150, earlier than that in ALL150 and CRU data set. The analysis of running interdecadal trends and simulated spatial differences in summer precipitation further confirms this point (Fig. 8a and b). The summer precipitation increases over the YRV, whereas it decreases over the NC from the period 1953–1972 to the period 1973–1990. The linear trends are $0.49\,\mathrm{mm\,day^{-1}}\ (40\,\mathrm{yr})^{-1}$ for the YRV ($P = 0.01$) and $-0.24\,\mathrm{mm\,day^{-1}}\ (40\,\mathrm{yr})^{-1}$ for the NC ($P = 0.10$) during the period of 1953–1990. It is suggested that there are some linkages between the anthropogenic forcing agents and the IVSP in ALL150 and the observation. Thus, this simulated IVSP during the period of 1953–1990 in ANT150 is used as a parallel analysis in the following study. In NAT150, nevertheless, the summer precipitation decreases over the YRV, but increases over the NC in the 1970s, further confirming the opposite precipitation trends over eastern China in NAT150 compared to other ensembles and observations.

Actually, the anomalous summer precipitation over the NC and YRV are not opposite to each other all the time (Fig. 7). In some periods, they are consistent for these two regions. The changes in summer precipitation over eastern China are very complex. Thus, in order to investigate how the external forcings affect summer precipitation over eastern China and the root causes of the IVSP in late 1970s, we first need to understand the key meteorological factors to influence the summer precipitation over the NC and YRV, respectively, particularly those related to the intrinsic variability of the climate system.

As shown in Fig. 9a, when summer precipitation increases over the NC, obvious southerly wind anomalies are evident over eastern China and they can reach north of 40° N. At the same time, an anomalously cyclonic circulation is observed in the low troposphere over the NC, implying strong convection there. Correspondingly, significant negative anomalies

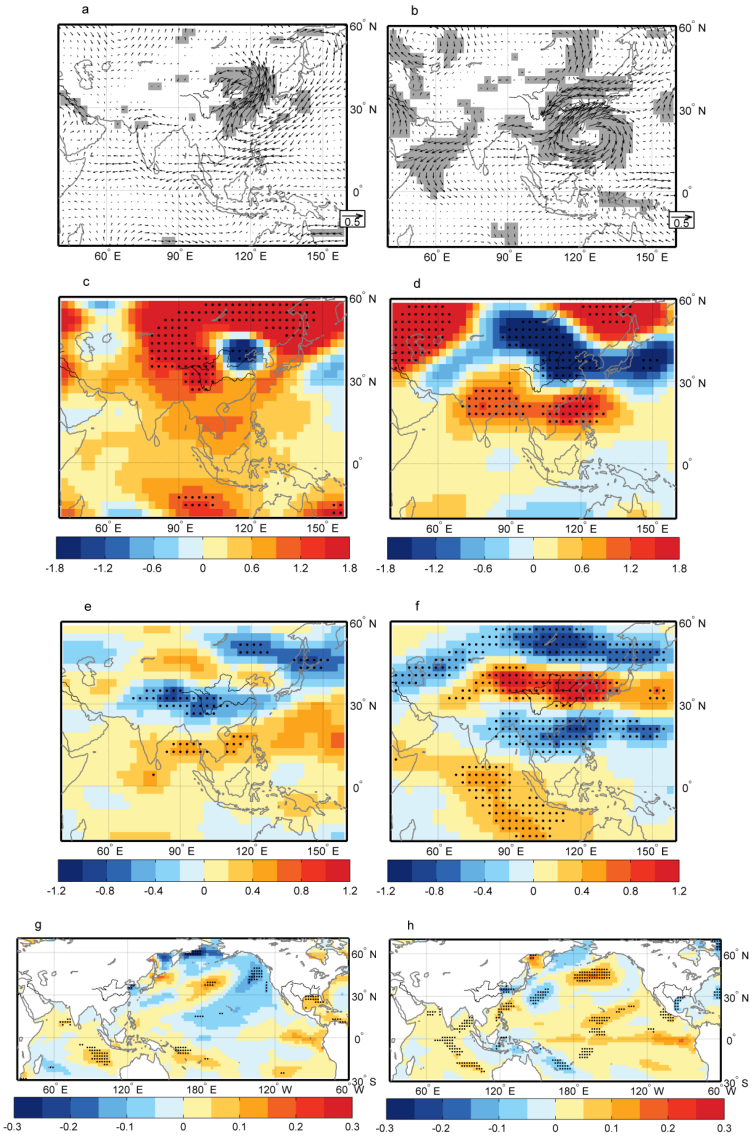

Fig. 9. Regression of summer (June-July-August) **(a, b)** 850 hPa wind (unit: $m\,s^{-1}$), **(c, d)** 500 hPa geopotential height (unit: m), **(e, f)** 200 hPa zonal wind (unit: $m\,s^{-1}$), and **(g, h)** sea surface temperature (unit: °C) on time series of summer precipitation anomalies (unit: $mm\,d^{-1}$) over the NC (left) and YRV (right) regions in CTL150. Areas with confidence level exceeding 95 % are shaded with gray or denoted with dots. Regions with elevations higher than 1500 m are blank in **(a)** and **(b)**.

in the 500 hPa geopotential height can be found over this region (Fig. 9c). In the upper troposphere, negative zonal wind anomalies appear along 30° N, indicating a weak and northward East Asia westerly jet (EAJ) over the continent (Fig. 9e). In this period, a negative PDO-like sea surface temperature (SST) pattern is observed over the North Pacific.

On the other hand, when the summer precipitation increases in the YRV, the southerly wind anomalies only extend south of 30° N (Fig. 9b), implying a relatively weak EASM. Differently from changes of summer precipitation in the NC, the anomalously cyclonic circulation over eastern China shifts southward and is located over the YRV region. The enhanced convection over the YRV is the direct factor that causes summer precipitation to increase there. In addition, the Somali jet is also markedly weakened. In the mid- and upper troposphere, the western Pacific subtropical high (WPSH) shifts westward, and the South Asia high (SAH) is strengthened. The positive–negative zonal wind anomalies at 200 hPa over the north and south sides of the Yangtze River imply a strengthened and southward EAJ when the summer precipitation is high over the YRV (Fig. 9f). For the SST, the positive anomalies can be found over the South China Sea, subtropical northwestern Pacific, and most parts of the

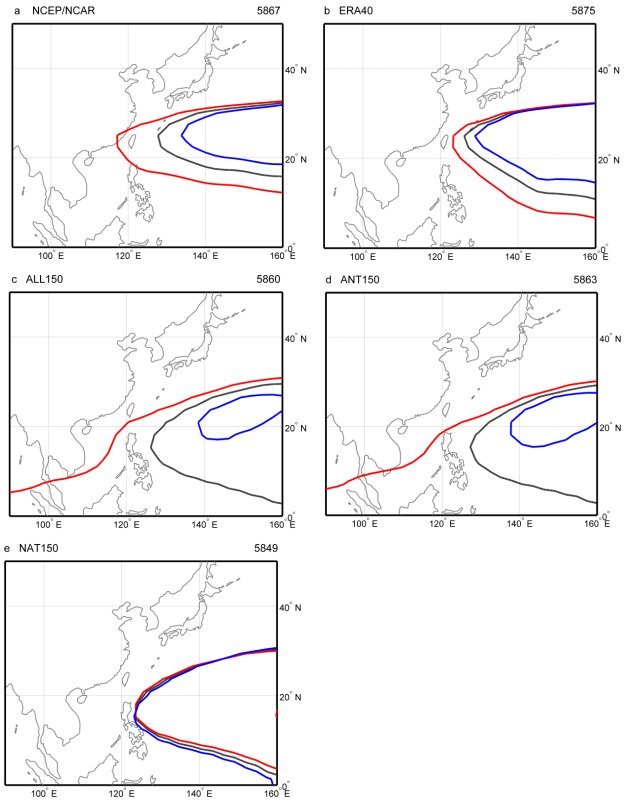

Fig. 10. The observed and simulated positions of characteristic western Pacific subtropical high isoline at 500 hPa during the periods 1978–1995 (red line), 1958–1977 (blue line) and 1958–1995 (black line) in the **(a)** NCEP/NCAR, **(b)** ERA40, **(c)** ALL150, **(d)** ANT150 (the corresponding periods 1973–1990, 1953–1972, and 1953–1990 in the ANT150), and **(e)** NAT150. The value of the western Pacific subtropical high isoline in each data is shown at the upper right corner (unit: m).

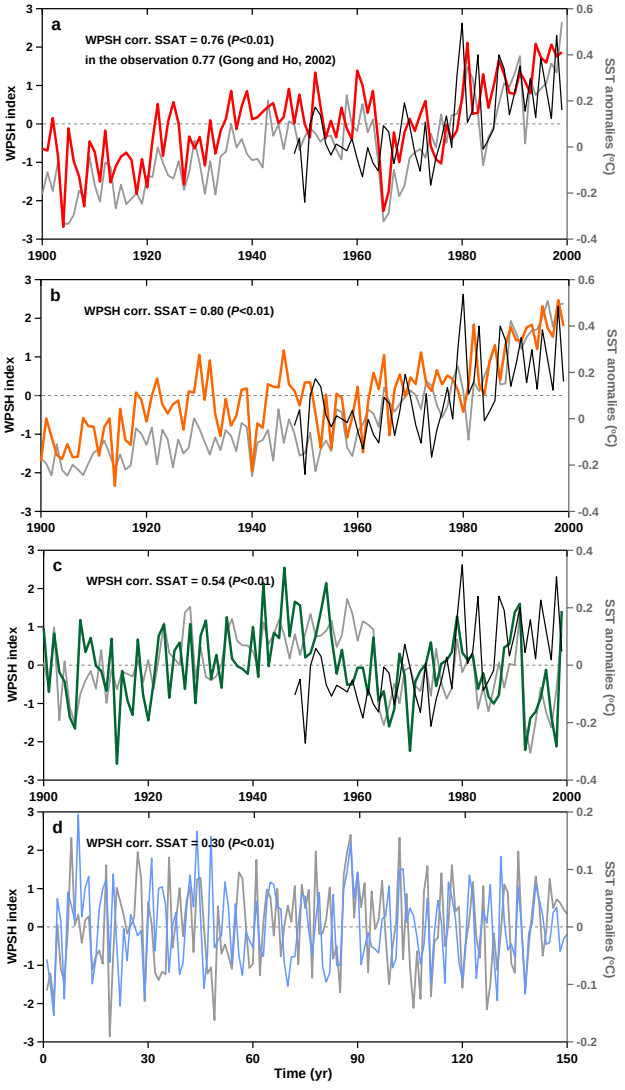

Fig. 11. Time series of simulated WPSH index (color lines) and Indian Ocean SST (gray lines, 20° S–20° N, 40–100° E) in **(a)** ALL150, **(b)** ANT150, **(c)** NAT150, and **(d)** CTL150. Black lines are for the WPSH index in NCEP/NCAR reanalysis data.

Indian Ocean (Fig. 9h), whereas negative anomalies over the northwestern Pacific.

These anomalies in the troposphere and surface are strongly tied to the changes in the summer precipitation over the NC and YRV. In the following we focus in particular on the responses of these meteorological factors to external forcings and try to explain how they couple together to cause the IVSP in eastern China in late 1970s.

3.3 Changes in western Pacific subtropical high and SST

The WPSH is an important component of the EASM system (Tao and Chen, 1987). The low-level jet along the western edge of the WPSH transports a large amount of water vapor into East Asia. Therefore, any changes in the WPSH would potentially influence precipitation over eastern China (Ninomiya and Kobayashi, 1999). Following Zhou et al. (2009), the climatological isoline (geopotential height at 500 hPa) for the whole period (1958–1995; 1953–1990 for ANT150) straddling the longitude of 130° E is defined as the characteristic WPSH isoline. As shown in Fig. 10, the black lines indicate the climatological position of the WPSH in the reanalysis data sets and numerical experiments, and their values of WPSH isoline are shown at the upper right corner. The red lines and blue lines indicate the positions of the WPSH during the periods of 1978–1995 and 1958–1977 (1973–1990 and 1953–1972 for ANT150).

Since the late 1970s, the WPSH has extended further west compared with the 1960s and 1970s. This significant interdecadal shift is also observed in the variation of the WPSH index (Fig. 11), which is defined as normalized anomalies of geopotential height at 500 hPa over the region (125–140° E, 20–25° N; He and Gong, 2002). As a result, the monsoon rain

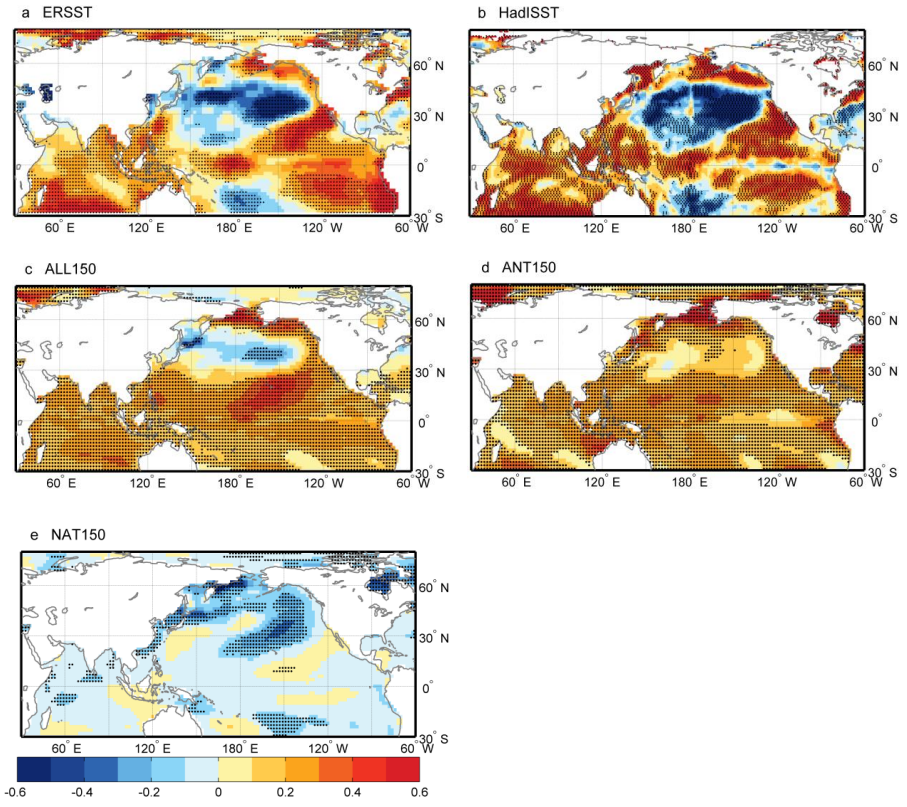

Fig. 12. The differences (1978–1995 minus 1958–1977) in the observed and simulated summer SST (June-July-August, unit: °C) in the **(a)** ERSST, **(b)** HadISST, **(c)** ALL150, **(d)** ANT150 (1973–1990 minus 1953–1972), and **(e)** NAT150. Areas with confidence level exceeding 90 % are denoted with dots.

belt has been pushed toward the YRV, resulting in more precipitation in this region (Gong and Ho, 2002; Zhou and Yu, 2005). This relationship between variation of summer precipitation over the YRV and that of the WPSH also can be found in CTL150 (Fig. 9d).

Both in ALL150 and ANT150, the simulated WPSH is pushed more westward in the latter decades of the 20th century (Fig. 10), although both simulations exaggerate these changes compared with the reanalysis data set. Thus, the simulated summer precipitation increases over the YRV in both ALL150 (Fig. 5c) and ANT150 (Fig. 8b) during this period. Besides, the interdecadal shift in WPSH happens earlier in ANT150 than that in ALL150 and observations (Fig. 11), which is likely the reason of the earlier increase in summer precipitation over the YRV in ANT150 mentioned before (Figs. 7 and 8). It is, however, hard to find such interdecadal shift in NAT150 during the second half of the 20th century and in the whole CTL150 simulation.

The ultimate cause of the westward extension of the WPSH, on an annual timescale, is the anomalous warming of the Indian Ocean. The increased SST over the Indian Ocean warms the tropical tropospheric air via deep convection adjustment. Then, the heated tropical troposphere, on the one hand, triggers an anticyclonic pattern over the northwestern Pacific though emanation of baroclinic Kelvin waves, intensifying the WPSH (Xie et al., 2009; also seen in Fig. 9b, d and h). On the other hand, it produces a positive height anomaly over South Asia, modifying the SAH (Huang et al., 2011). The intensified SAH causes a further westward extension of the WPSH through emanating anomalous wave energy downstream along the westerly jet (Zhao et al., 2009), making the WPSH and the SAH vary synchronously (Tao and Zhu, 1964; Jiang et al., 2011; also seen in Fig. 9b). Therefore, the variation of the Indian Ocean SST plays an important role in affecting the WPSH. The strong correlations between them in the observation (0.77 according to Gong and Ho, 2002) and the BCM ensemble results further confirm this point (Fig. 11). Modeling studies (Zhou et al., 2009) and observational evidence (Gong and Ho, 2002) also suggest that, on interdecadal timescales, this relationship does exist.

As shown in the observed SST (Fig. 12), significant basin-wide SST warming can be found in the Indian Ocean, South China Sea and tropical western Pacific during the period 1978–1995. In addition, a warm PDO-like SST pattern emerged in the North Pacific during this period. Large-scale anomalously negative SSTs are evident over the west-central North Pacific, whereas positive SSTs are located over the high-latitude North Pacific and along the west coast of North

America. In the BCM, these observed differences in the SST warming–cooling conditions are well captured by ALL150 and partly captured by ANT150, while NAT150 failed to capture these anomalies. It is indicated that, forced by the anthropogenic agent (i.e., increased greenhouse gas concentrations), the BCM realistically reproduced the Indian Ocean persistent warming, which ultimately caused the westward extension of the WPSH over the past few decades (also seen in Fig. 11). In addition, natural forcing or intrinsic climate variability is incapable of causing such observed large-scale changes in the SST and WPSH during the second half of the 20th century.

It is interesting to note that the natural forcing weakens the WPSH by cooling the Indian Ocean SST during the second half of the 20th century (Fig. 11c), mainly on an interannual timescale. That means the natural forcing can to some extent mitigate the anthropogenically induced Indian Ocean warming, causing the delayed shift in the WPSH in ALL150 compared with ANT150. In addition, the correlations between the Indian Ocean SST and WPSH in ALL150, ANT150 and NAT150 are much higher than that in CTL150. It is likely because the external-forcing-induced decadal changes strengthen the covariance of the Indian Ocean SST and the WPSH, as pointed out by Gong and Ho (2002).

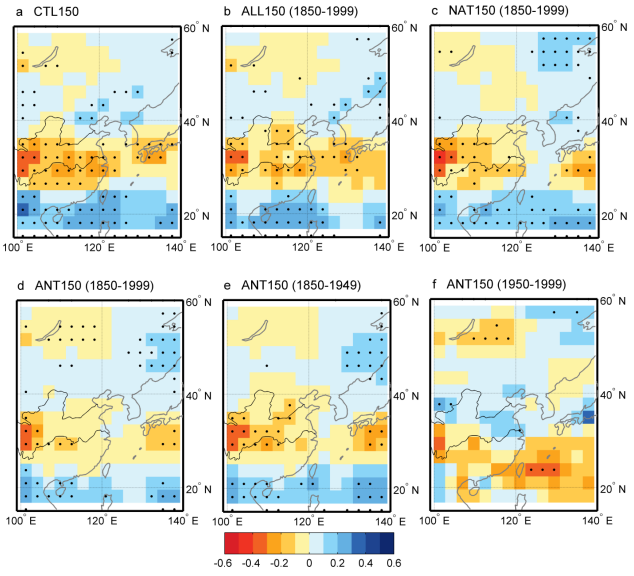

Fig. 13. Regression of summer (June-July-August) precipitation (unit: mm d^{-1}) on time series of EAJ index in **(a)** CTL150, **(b)** ALL150, **(c)** NAT150, **(d)** ANT150 (1850–1999), **(e)** ANT150 (1850–1949), and **(f)** ANT150 (1950–1999). Areas with confidence level exceeding 95 % are denoted with dots.

3.4 Changes in East Asia westerly jet

The EAJ is another important component of the EASM system, which is often located between 20° N and 50° N over East Asia during the boreal summer. On its south side, the EAJ can lead to the divergence in the upper troposphere and, consequently, cause a strong ascending motion and convergence in the lower troposphere. Thus, the variation of the EAJ is closely linked to monsoon precipitation over East Asia (Liang and Wang, 1998). In order to examine the variation of the meridional displacement of the EAJ and its impact on the summer precipitation over eastern China, an axis index of the EAJ is analyzed here, which is defined as the normalized mean location (latitude) of the 200 hPa maximum westerly at various longitudes over East Asia (70–120° E, 30–50° N; Kuang and Zhang, 2006). The higher value of this index (i.e., a northward displacement of EAJ) corresponds to a decrease in summer precipitation over the YRV region in the observation (Kuang and Zhang, 2006) and BCM ensemble simulations (Fig. 13), and vice versa. It is interesting to find that the relationship between the EAJ index and summer precipitation is much weaker in ANT150. And this significantly weakened covariance of them mainly happens during the period of 1950–1999 in this ensemble (Fig. 13d, e and f).

Figures 14 and 15 show the changes in 200 hPa zonal winds between the periods of 1978–1995 and 1958–1977 (1973–1990 and 1953–1972 for ANT150) and the time evolution of the EAJ index for the 20th century, respectively. In the reanalysis data, anomalously negative zonal winds are evident over northern East Asia, whereas positive ones are located over the southern parts. This dipole mode in zonal wind anomalies, together with changes in EAJ index, indicates a long-term southward EAJ during the latter period. Compared with reanalysis data, ALL150 well captures this anomalous mode and the interdecadal shift in the EAJ index since the late 1970s, which can contribute to the increased summer precipitation over the YRV.

In ANT150, a similar dipole mode is also observed over East Asia, but shifted southward about 10 degrees compared with reanalysis data and ALL150. This implies a strong southward displacement of the EAJ during the latter period, which is likely the reason for the increase in precipitation over South China in ANT150 (Fig. 8b). On the other hand, the EAJ index in ANT150 decreases much earlier, even from the 1950s forced by the anthropogenic agent (Fig. 15b). This partly explains the covariance between the EAJ index and summer precipitation over the region shifting from the YRV to South China in ANT150 during the second half of the 20th century (Fig. 13e and f).

In NAT150, it is hard to see any anomalous interdecadal signals (Fig. 14e). However, an earlier shift also can be found in the EAJ index. Since the 1960s, the EAJ index has been predominately positive and higher than that during the early 20th century (Fig. 15c). The mean value (1950–1999) is 0.14 in NAT150, which is opposite to that in ANT150 (−0.16). This means the natural forcing tends to displace the EAJ further northward during the second half of the 20th century compared to the early 20th century.

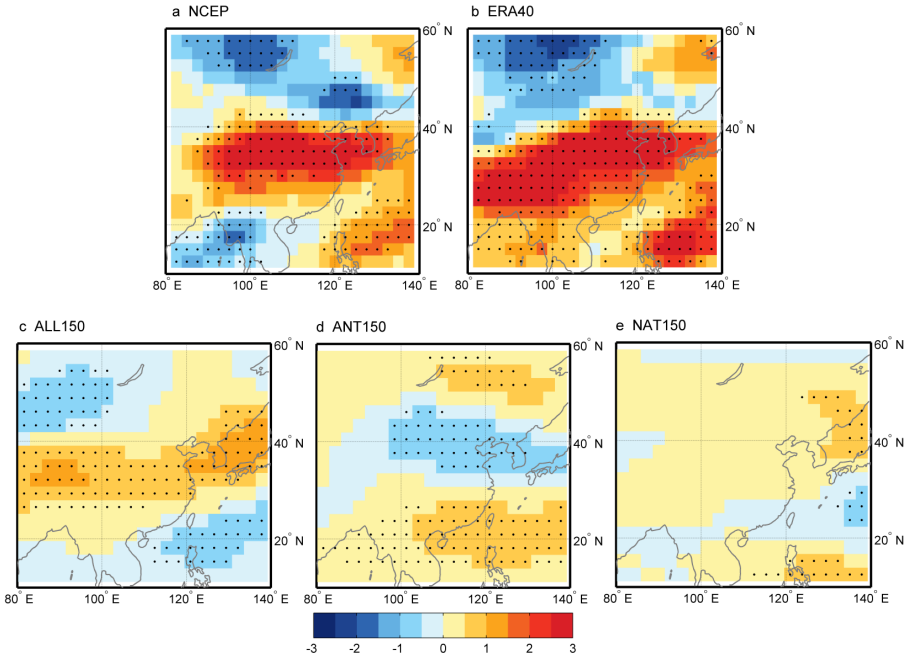

Fig. 14. The differences (1978–1995 minus 1958–1977) in summer zonal wind fields at 200 hPa (June-July-August, unit: $m\,s^{-1}$) in the **(a)** NCEP/NCAR, **(b)** ERA40, **(c)** ALL150, **(d)** ANT150 (1973–1990 minus 1953–1972), and **(e)** NAT150. Areas with confidence level exceeding 90 % are denoted with dots.

In the subtropics and mid-latitudes, wind and geopotential height follow the quasi-geostrophic equilibrium. As a result, the anomalous geopotential height over the tropics plays an important role on the meridional displacement of the subtropical and mid-latitude westerly jet. For the Asian summer monsoon region, the Indian Ocean SST is a notable tropical surface forcing. As shown in Fig. 16, when the Indian Ocean SST increases (decreases), positive (negative) westerly anomalies are located over the subtropics, implying a southward (northward) displaced EAJ. Based on observational data, Qu and Huang (2012) also addressed the relationship between the Indian Ocean SST and EAJ, and pointed out one possible mechanism as follows: the anomalously warm SSTs over the Indian Ocean heat the overlying tropospheric air and lead to anomalous convection, which forces a Kelvin wave wedge penetrating into the equatorial western North Pacific (Xie et al., 2009). Combined with the climatological easterly shear over the subtropical western North Pacific, the East Asia–Pacific teleconnection is induced along the East Asia coast (Lu, 2004). The East Asia–Pacific-related upper-level anomalous cyclone accelerates westerly in the south flank of EAJ and decelerates westerly in the north flank. Finally, the EAJ shifts southward. In contrast, the EAJ shifts northward when the Indian Ocean SST is lower than normal. Therefore, the BCM ensemble simulations (Fig. 16) and previous observational studies both indicate that influences from different Indian Ocean SST play a substantial role in the displacement of the EAJ, further regulating the summer precipitation over eastern China. Furthermore, through the warming (cooling) of the Indian Ocean, the anthropogenic (natural) forcing agent is the root cause of the southward (northward) displacement of the EAJ for the period of 1950–1999 in the ANT150 and NAT150 simulations, respectively.

3.5 Changes in lower tropospheric monsoon circulation

The weakening of the Asian monsoon circulation has been suggested to be an important factor for the IVSP over eastern China in the late 1970s (Ding et al., 2009). Here we therefore examine some key aspects of the observed and simulated EASM circulation for the late 20th century. In the observations, significant positive sea level pressure (SLP) anomalies are evident over East Asia, while slightly negative anomalies can be seen over the northwestern Pacific and high-latitude regions (Fig. 17a). In the reanalysis data sets, the positive SLP anomalies in NCEP/NCAR reach 6 hPa (Fig. 17b), which are much larger than those from the observation (1.2 hPa) and ERA40 (3 hPa, Fig. 17c). The ERA40 data are more consistent with observations than the NCEP/NCAR data. The large-scale anomalies in SLP lead to anomalous northerly winds over eastern China (Fig. 18a and b). At the same time, both the southwestern flow from South Asia and the cross-equatorial flow from Southeast Asia are weakened, implying a weaker Asian summer monsoon circulation during the period 1978–1995. It should be noted that the changes in the wind fields are much larger in the NCEP/NCAR data than those in the ERA40 data, as should be expected from the

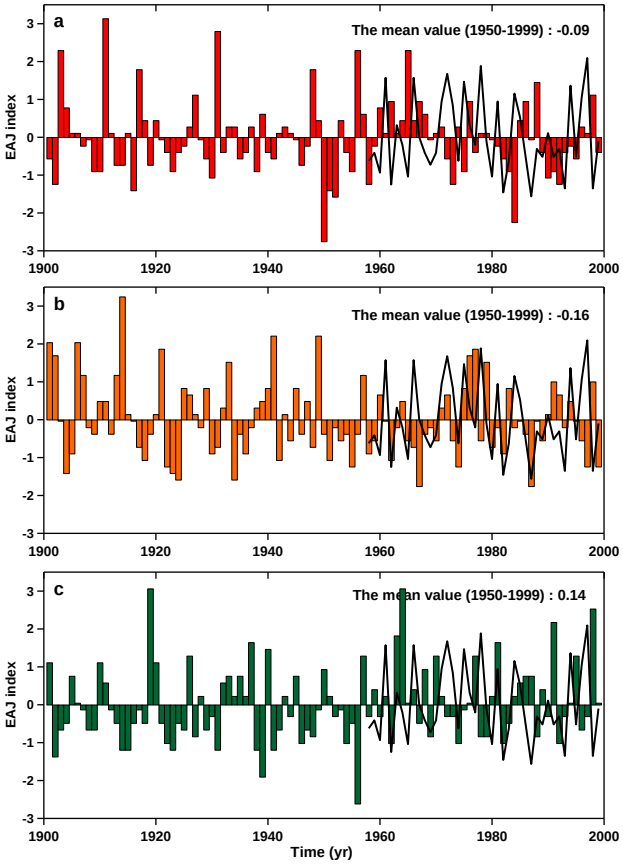

Fig. 15. Time series of simulated EAJ index (color histograms) in **(a)** ALL150, **(b)** ANT150, and **(c)** NAT150. Black lines are for the EAJ index in NCEP/NCAR reanalysis data.

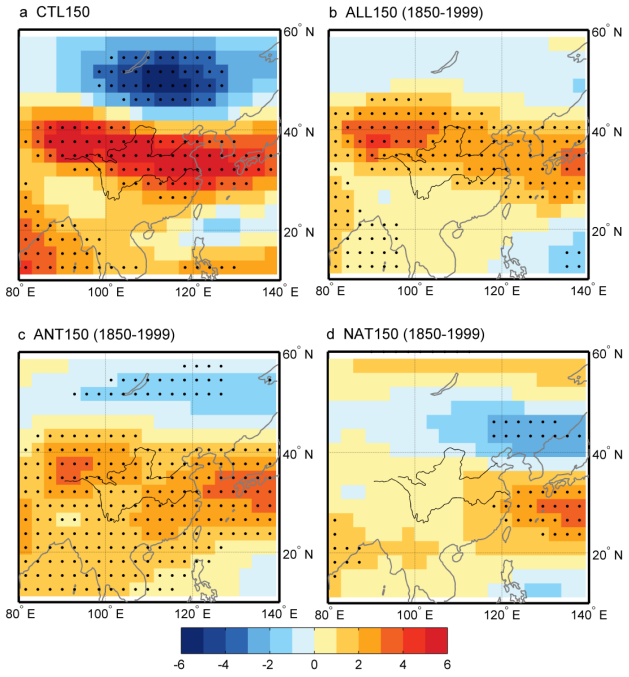

Fig. 16. Regression of summer zonal wind fields at 200 hPa (June-July-August, unit: $m\,s^{-1}$) on time series of summer Indian Ocean SST (20° S–20° N, 40–100° E) in **(a)** CTL150, **(b)** ALL150, **(c)** ANT150, and **(d)** NAT150. Areas with confidence level exceeding 95 % are denoted with dots.

anomalously large, positive SLP values in the NCEP/NCAR data compared with observations. The NCEP/NCAR data overestimate the interdecadal changes over Asia, as indicated by Wu et al. (2005). However, both NCEP/NCAR and ERA40 show significantly weakened EASM during the period 1978–1995 relative to the period 1958–1977.

In the model (Figs. 17 and 18), ALL150 realistically reproduced the increased SLP over the Asian continent and the weakened Asian summer monsoon circulations. These observed climatic features were partly captured by ANT150. In addition, anomalously cyclonic circulations are observed over the YRV in ALL150 and ANT150, implying stronger convection there. They are the major factors that contribute to the increased summer precipitation over the YRV in these two ensembles (also seen in Fig. 9b). In contrast, NAT150 failed to reproduce these climate changes. Also, positive SLP anomalies are evident over the South China Sea, which actually enhance the EASM. Therefore, NAT150 simulates the increased summer precipitation over the NC and decreased precipitation over the YRV, showing opposite trends compared to the other ensembles and the observations (Figs. 5, 6 and 7).

Generally, the intensity of the EASM is controlled by the thermal contrast between land and ocean (Webster, 1987; Tao and Chen, 1987). In the observations, strong negative temperature anomalies are found over eastern China (Fig. 19a and b), with positive temperature anomalies in the surrounding regions. This distribution of temperature anomalies has been suggested to reduce meridional and zonal land–sea thermal contrasts and by that to weaken the EASM (Zuo et al., 2012).

Unlike the observations, the simulated anomalous temperature pattern in NAT150 shows large-scale cooling over East Asia for the period 1978–1995 (Fig. 19e), likely as a result of the El Chichón and Mount Pinatubo volcanic eruptions in 1982 and 1991, respectively (Fig. 20a and b). Together with the Agung eruption in 1963, these strong volcanic eruptions in the second half of the 20th century to some extent mitigated the greenhouse-gas-induced warming.

In ALL150, the simulated temperature anomaly pattern qualitatively matches the observations (Fig. 19c). According to ANT150 (Fig. 19d), the significant warm anomalies over East Asia and the surrounding oceans are presumably caused by increased greenhouse gas concentrations. On the other hand, the slight cooling and the less pronounced warming over the mid- and high-latitude East Asian continent in ALL150 is likely attributed to the natural forcing. Others over eastern China (black box in Fig. 19) are partly caused by the response of land surface to enhanced convection. The

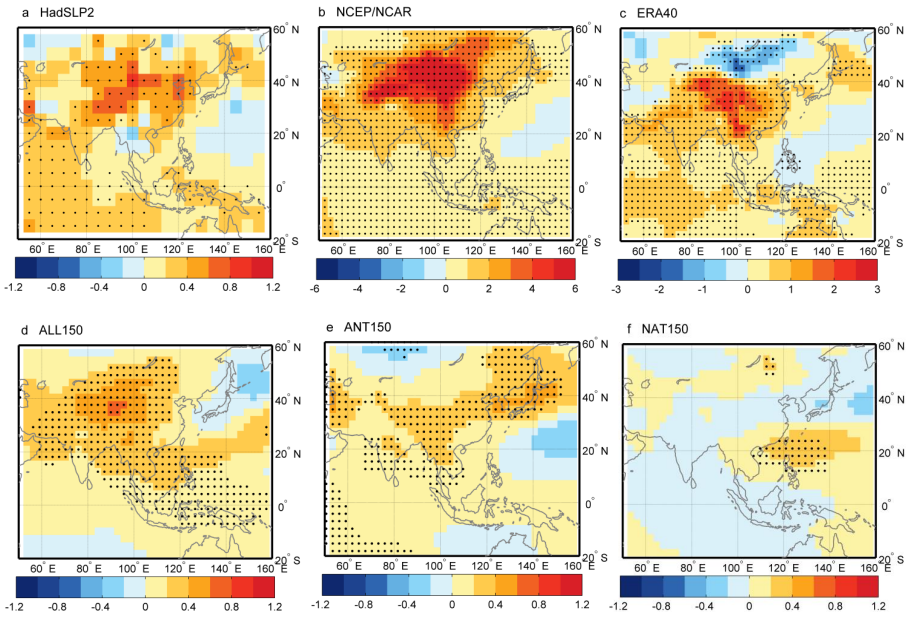

Fig. 17. The differences (1978–1995 minus 1958–1977) in summer sea level pressure (June-July-August, unit: hPa) in the **(a)** HadSLP2, **(b)** NCEP/NCAR, **(c)** ERA40, **(d)** ALL150, **(e)** ANT150 (1973–1990 minus 1953–1972), and **(f)** NAT150. Areas with confidence level exceeding 90 % are denoted with dots.

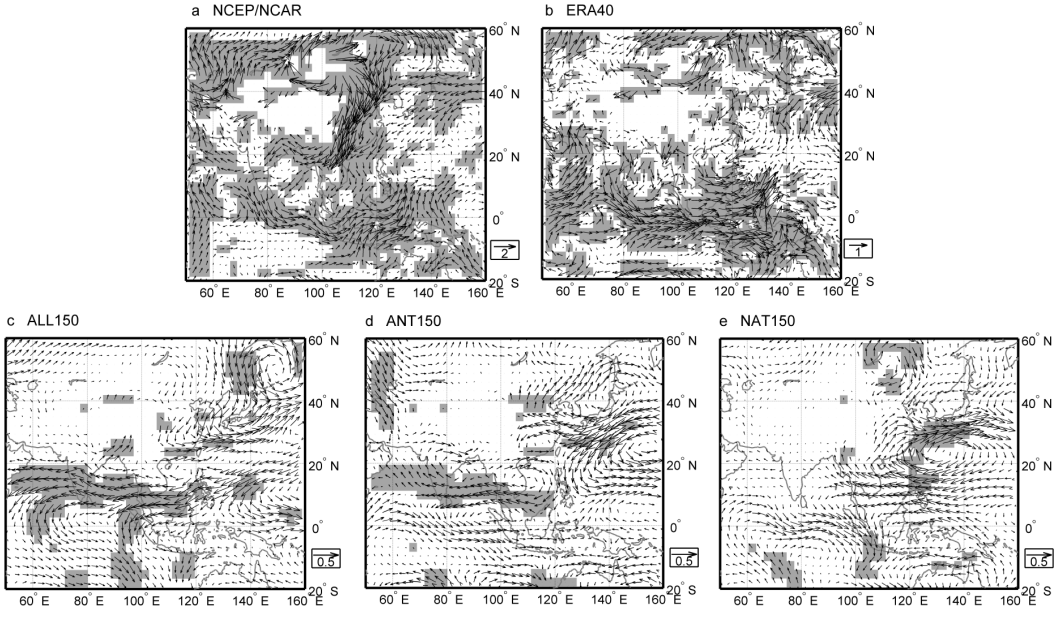

Fig. 18. The differences (1978–1995 minus 1958–1977) in summer wind fields at 850 hPa (June-July-August, unit: $m\,s^{-1}$) in the **(a)** NCEP/NCAR, **(b)** ERA40, **(c)** ALL150, **(d)** ANT150 (1973–1990 minus 1953–1972), and **(e)** NAT150. Areas with confidence level exceeding 90 % are shaded with gray. Regions with elevations higher than 1500 m are blank.

enhanced convection can reflect more shortwave radiation and cool the surface. Meanwhile, the increased summer precipitation over the YRV in ALL150 also strengthens surface evaporative cooling there. Besides, the cooling effect of the anthropogenic aerosol is not negligible either (Liao et al., 2004; T. J. Wang et al., 2010; Li et al., 2011). Unlike the greenhouse gases, the distribution of anthropogenic aerosols is spatially uneven and usually centered over industrial areas such as eastern China (Fig. 2). Kaiser and Qian (2002) indicated that the dimming effect of rapidly

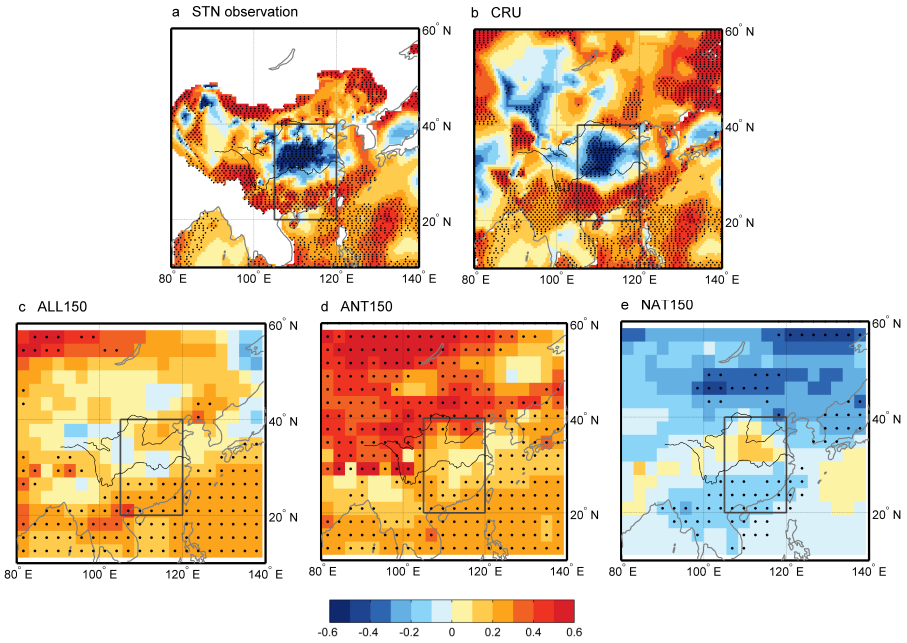

Fig. 19. The differences (1978–1995 minus 1958–1977) in summer surface air temperature (June-July-August, unit: °C) in the **(a)** STN data, **(b)** CRU data set, **(c)** ALL150, **(d)** ANT150 (1973–1990 minus 1953–1972), and **(e)** NAT150. In **(a)** and **(b)**, the corresponding differences in SST (HadISST) are shaded over the ocean. Areas with confidence level exceeding 90 % are denoted with dots. The box denotes the analysis region dominated by East Asian summer monsoon (20–40° N, 105–120° E), over which the average temperature over land is calculated.

increasing anthropogenic aerosols could have played an important role in the cooling trend over eastern China after 1980 based on observational data. Thus, the cooling effect of the anthropogenic aerosols can also contribute to the cooling and the less pronounced warming over eastern China in ALL150 and ANT150. In addition, it should be noted that only sulfate aerosols have been included in this study. The potential effects of other reflecting aerosol species, such as nitrate aerosols, on the regional temperature evolution over the Asian continent have therefore not been considered. This may be one reason why ALL150 and ANT150 simulate weaker interdecadal temperature changes relative to the observations over eastern China.

Therefore, in ALL150, the cooling (or the less pronounced warming) eastern China and significant warming ocean play an important role in reducing land–sea thermal contrasts over East Asia. Together with the influences from a westward WPSH and a southward EAJ, they all contribute to the lower tropospheric weakened EASM, thereby causing the decrease in summer precipitation over the NC as found in the observation.

4 Summary and discussion

The model results presented here, together with observations, suggest that anthropogenic forcings are most likely the prime drivers for the IVSP over eastern China in the late 1970s. The increased greenhouse gas concentrations induced Indian Ocean warming causing a westward shift of the WPSH and a southward displacement of the EAJ, which ultimately led to enhanced water vapor transport and summer precipitation over the YRV region. At the same period, the surface cooling effects from the stronger convection, higher precipitation and rapidly increasing anthropogenic aerosols led to the negative temperature anomalies over eastern China. It is in stark contrast with the surrounding warming ocean caused by the increased greenhouse gases, resulting in reduced land–sea thermal contrasts. By the cooperation of the westward-shifted WPSH, the southward-shifted EAJ and reduced land–sea thermal contrasts, the EASM weakened and the summer precipitation deceased over the NC. Consequently, the IVSP started to emerge in eastern China in the late 1970s. This study highlights the dominant roles of anthropogenic forcings in the interdecadal changes of the East Asian climate during the second half of the 20th century.

In addition, the external natural forcing plays an opposite role to the anthropogenic forcing in regulating the changes in WPSH and EAJ and mitigating the surrounding ocean warming of eastern China, and postpones the anthropogenically forced IVSP and associated climate changes in eastern China in ALL150 during the second half of the 20th century. This is likely the reason why ALL150 compares so well with the observations. The model results therefore clearly underline the need to include all relevant anthropogenic and natural forcings in order to get the correct timing of the simulated

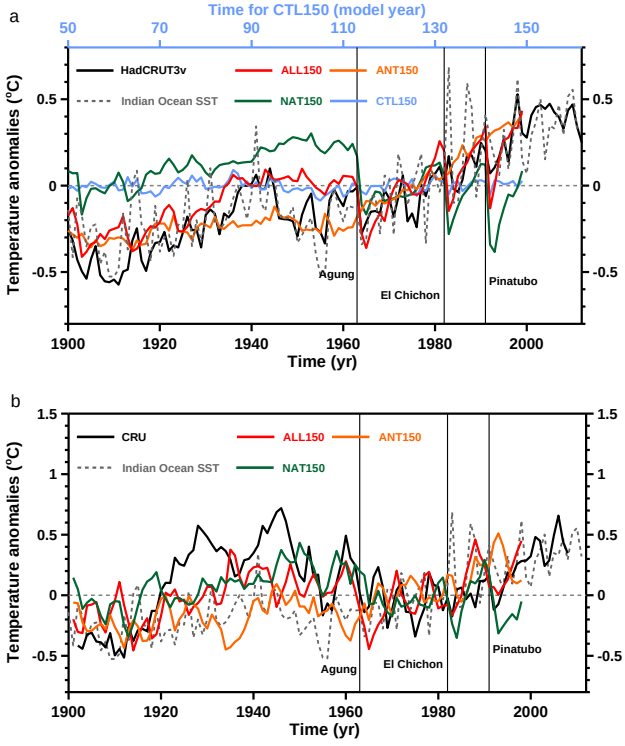

Fig. 20. Time series of **(a)** the annual global-mean surface air temperature anomalies (unit: °C) and **(b)** 3 yr running mean summer surface air temperature anomalies over eastern China (unit: °C, 20–40° N, 105–120° E; see the black box in Fig. 19), relative to the 1961–1990 average, for the HadCRUT3v observational data set, CRU data set and ensemble model results. The gray lines in **(a)** and **(b)** are the summer Indian Ocean SST anomalies (unit: °C, 20° S–20° N, 40–100° E) in HadISST data set.

shift in the East Asian climate over the past few decades. Moreover, the simulated responses in the different forced ensembles cannot be added together linearly, suggesting that complex non-linear processes are likely involved in the atmospheric response to all relevant anthropogenic and natural forcings.

Recently, Chen et al. (2012) used an atmosphere model forced by observed historical SSTs and fixed emissions scenarios at the 1990 level to reproduce a similar precipitation trend over eastern China, but their results are not able to separate the effects of the anthropogenic and natural forcings. However, Chen et al. (2012) still highlight the important role of anomalous SST forcing on the East Asian summer precipitation, as pointed out by Y. Wang and Yan (2011) and T. Wang and H. J. Wang (2013). Additionally, a significant statistical relationship between the PDO and dry/wet variation of the NC region in the observation (Ma and Shao, 2006) and BCM 600 yr control run (L. Yu et al., personal communication, 2013) implies that the influence of the PDO on the precipitation in eastern China is not negligible. This means that the shift of the PDO into a positive phase during the late 20th century could further contribute to the drying condition in the NC, which partly explains the weak NC drying when no PDO signals are found in ANT150 (Fig. 8b and 12d). In our model results, the BCM does in fact a remarkable good job in reproducing the decadal SST variability over the North Pacific (i.e., PDO) and the Indian Ocean warming during the second half of the 20th century (Fig. 12c). This may be a key reason why the BCM ALL150 ensemble can successfully reproduce the weakened EASM and the IVSP over eastern China during the late 20th century.

In the last 10 yr, the annual-mean global temperature has not risen (Fig. 20a; Easterling and Wehner, 2009; Foster and Rahmstorf, 2011), despite the continued increased anthropogenic forcing. A recent study tied this current hiatus in global warming specifically to a La Niña-like decadal cooling, a strong intrinsic climate variability, in the eastern tropical Pacific (Kosaka and Xie, 2013). This decadal cooling could further regulate the Indian Ocean SST through air–sea interaction (Du et al., 2009). Thus, a similar hiatus in SST warming can also be seen in the Indian Ocean (Fig. 20a). However, the warming caused by greenhouse gases in the mid- and high-latitude regions (Kosaka and Xie, 2013) and eastern China (Fig. 20b) continued in the boreal summer during this period. That means the heat forcing over the Indian Ocean will be relatively weak during this period, in contrast to the strong heat forcing that is seen in the second half of the 20th century. This is one potential explanation for why the southern flood and northern drought pattern in eastern China has reversed in the last 10 yr.

Acknowledgements. We sincerely thank two anonymous reviewers and Editor Q. Fu for their useful comments and suggestions, which helped to improve the quality of the paper significantly. We are grateful to J. Sun, D. Jiang, and Y. Zhu for fruitful discussions. The first author would like to thank Editor Q. Fu for his support and encouragement. This work was supported by the Major State Basic Research Development Program of China (973 Program) under grant no. 2009CB421406, the strategic Priority Research Program (XDA05120703, XDA05110203) of the Chinese Academy of Sciences, and Research Council of Norway through the DecCen project (Exploring Decadal to Century Scale Variability and Changes in the East Asian Climate during the last Millennium). This study is also a contribution to the Centre for Climate Dynamics at the Bjerknes Centre.

Edited by: Q. Fu

References

Allan, R. and Ansell, T.: A new globally complete monthly historical gridded mean sea level pressure dataset (HadSLP2): 1850–2004, J. Climate, 19, 5816–5842, 2006.

Bleck, R. and Smith, L. T.: A Wind-Driven Isopycnic Coordinate Model of the North and Equatorial Atlantic-Ocean. 1. Model Development and Supporting Experiments, J. Geophys. Res.-Oceans, 95, 3273–3285, 1990.

Bleck, R., Rooth, C., Hu, D. M., and Smith, L. T.: Salinity-Driven Thermocline Transients in a Wind-Forced and Thermohaline-Forced Isopycnic Coordinate Model of the North-Atlantic, J. Phys. Oceanogr., 22, 1486–1505, 1992.

Bollasina, M. A., Ming, Y., and Ramaswamy, V.: Anthropogenic aerosols and the weakening of the South Asian summer monsoon, Science, 334, 502–505, doi:10.1126/science.1204994, 2011.

Boucher, O. and Pham, M.: History of sulfate aerosol radiative forcings, Geophys. Res. Lett., 29, 1308, doi:10.1029/2001gl014048, 2002.

Chen, H. M., Yu, R. C., Li, J., Xin, X. G., Wang, Z. Z., and Wu, T. W.: The coherent interdecadal changes of East Asia climate in mid-summer simulated by BCC_AGCM 2.0.1, Clim. Dynam., 39, 155–163, doi:10.1007/s00382-011-1154-6, 2012.

Collins, M., Botzet, A., Carril, A. F., Drange, H., Jouzeau, A., Latif, M., Masina, S., Otteraa, O. H., Pohlmann, H., Sorteberg, A., Sutton, R., and Terray, L.: Interannual to decadal climate predictability in the North Atlantic: A multimodel-ensemble study, J. Climate, 19, 1195–1203, 2006.

Crowley, T. J., Baum, S. K., Kim, K. Y., Hegerl, G. C., and Hyde ,W. T.: Modeling ocean heat content changes during the last millennium, Geophys. Res. Lett., 30, 1932, doi:10.1029/2003gl017801, 2003.

Déqué, M., Dreveton, C., Braun, A., and Cariolle, D.: The Arpege/Ifs Atmosphere Model – a Contribution to the French Community Climate Modeling, Clim. Dynam., 10, 249–266, 1994.

Ding, Y. H.: Summer Monsoon Rainfalls in China, J. Meteorol. Soc. Jpn., 70, 373–396, 1992.

Ding, Y. H. and Chan, J. C. L.: The East Asian summer monsoon: an overview, Meteorol. Atmos. Phys., 89, 117–142, doi:10.1007/s00703-005-0125-z, 2005.

Ding, Y. H., Wang, Z. Y., and Sun, Y.: Inter-decadal variation of the summer precipitation in East China and its association with decreasing Asian summer monsoon. Part I: Observed evidences, Int. J. Climatol., 28, 1139–1161, doi:10.1002/Joc.1615, 2008.

Ding, Y. H., Sun, Y., Wang, Z. Y., Zhu, Y. X., and Song, Y. F.: Inter-decadal variation of the summer precipitation in China and its association with decreasing Asian summer monsoon Part II: Possible causes, Int. J. Climatol., 29, 1926–1944, doi:10.1002/Joc.1759, 2009.

Du, Y., Xie, S. P., Huang, G., and Hu, K.: Role of air-sea interaction in the long persistence of El Niño-induced north Indian Ocean warming, J. Climate, 22, 2023–2038, 2009.

Easterling, D. R. and Wehner, M. F.: Is the climate warming or cooling?, Geophys. Res. Lett., 36, L08706, doi:10.1029/2009GL037810, 2009.

Foster, G. and Rahmstorf, S.: Global temperature evolution 1979–2010, Environ. Res. Lett., 6, 044022, doi:10.1088/1748-9326/6/4/044022, 2011.

Furevik, T., Bentsen, M., Drange, H., Kindem, I., Kvamst , N., and Sorteberg, A.: Description and evaluation of the Bergen climate model: ARPEGE coupled with MICOM, Clim. Dynam., 21, 27–51, 2003.

Gong, D. Y. and Ho, C. H.: Shift in the summer rainfall over the Yangtze River valley in the late 1970s, Geophys. Res. Lett., 29, 1436, doi:10.1029/2001gl014523, 2002.

Gong, D. Y. and Ho, C. H.: Arctic oscillation signals in the East Asian summer monsoon, J. Geophys. Res.-Atmos., 108, 4066, doi:10.1029/2002jd002193, 2003.

He, X. Z. and Gong, D. Y., Interdecadal change in Western Pacific Subtropical High and climatic effects, J. Geogr. Sci., 12, 202–209, 2002.

Hegerl, G. C., Zwiers, F. W., Praconnot, P., Gillett, N. P., Luo, Y., Marengo Orsini, J. A., Nicholls, N., Penner, J. E., and Stott, P. A.: Understanding and Attributing Climate Change, in: Climate Change 2007: The Physical Science Basis. Contribution of Working Group I to the Fourth Assessment Report of the Intergovernmental Panel on Climate Change, edited by: Solomon, S., Qin, D., Manning, M., Chen, Z., Marquis, M., Averyt, K. B., Tignor, M., and Miller, H. L., Cambridge University Press, Cambridge, United Kingdom and New York, NY, USA, 2007.

Huang, G., Qu, X., and Hu, K.: The Impact of tropical Indian Ocean SST on South Asian High in Boreal Summer, Adv. Atmos. Sci., 28, 421–432, 2011

Huber, M. and Knutti, R.: Anthropogenic and natural warming inferred from changes in Earth's energy balance, Nat. Geosci., 5, 31–36, doi:10.1038/ngeo1327, 2012.

Jiang, D. B. and Wang, H. J.: Natural interdecadal weakening of East Asian summer monsoon in the late 20th century, Chinese Sci. Bull., 50, 1923–1929, doi:10.1360/982005-36, 2005.

Jiang, X. W., Li, Y. Q., Yang, S., and Wu, R. G.: Interannual and interdecadal variations of the South Asian and western Pacific subtropical highs and their relationships with Asian-Pacific summer climate, Meteorol. Atmos. Phys., 113, 171–180, 2011.

Johns, T., Royer, J. F., Höschel, I., Huebener, H., Roeckner, E., Manzini, E., May, W., Dufresne, J. L., Otterå, O., and van Vuuren, D.: Climate change under aggressive mitigation: the ENSEMBLES multi-model experiment, Clim. Dynam., 37, 1975–2003, 2011

Kaiser, D. P. and Qian, Y.: Decreasing trends in sunshine duration over China for 1954–1998: indication of increased haze pollution?, Geophys. Res. Lett., 29, 2042, doi:10.1029/2002gl016057, 2002.

Kalnay, E., Kanamitsu, M., Kistler, R., Collins, W., Deaven, D., Gandin, L., Iredell, M., Saha, S., White, G., Woollen, J., Zhu, Y., Chelliah, M., Ebisuzaki, W., Higgins, W., Janowiak, J., Mo, K. C., Ropelewski, C., Wang, J., Leetmaa, A., Reynolds, R., Jenne, R., and Joseph, D.: The NCEP/NCAR 40-year reanalysis project, B. Am. Meteorol. Soc., 77, 437–471, 1996.

Kosaka, Y. and Xie, S. P.: Recent global-warming hiatus tied to equatorial Pacific surface cooling, Nature, 501, 403–407, 2013.

Kuang, X. Y. and Zhang, Y. C.: Impact of the position abnormalities of East Asian subtropical westerly jet on summer precipitation in middle-lower reaches of Yangtze River, Plateau Meteorology, 25, 382–389, 2006.

Lefohn, A. S., Husar, J. D., and Husar, R. B.: Estimating historical anthropogenic global sulfur emission patterns for the period 1850–1990, Atmos. Environ., 33, 3435–3444, 1999.

Li, Z. Q., Li, C., Chen, H., Tsay, S. C., Holben, B., Huang, J., Li, B., Maring, H., Qian, Y., Shi, G., Xia, X., Yin, Y., Zheng, Y., and Zhuang, G.: East Asian Studies of Tropospheric Aerosols and their Impact on Regional Climate (EAST-AIRC): an overview, J. Geophys. Res.-Atmos., 116, D00K34, doi:10.1029/2010jd015257, 2011.

Liang, X. Z. and Wang, W. C.: Association between China monsoon rainfall and tropospheric jets, Q. J. Roy. Meteor. Soc., 124, 2597–2623, 1998.

Liao, H., Seinfeld, J. H., Adams, P. J., and Mickley, L. J.: Global radiative forcing of coupled tropospheric ozone and aerosols in a unified general circulation model, J. Geophys. Res.-Atmos., 109, D16207, doi:10.1029/2003jd004456, 2004.

Lu, R. Y.: Associations among the components of the East Asian summer monsoon system in the meridional direction, J. Meteorol. Soc. Jpn, 82, 155–165, 2004.

Ma, Z. G. and Shao, L. J.: Relationship between dry/wet variation and the Pacific Decade Oscillation (PDO) in northern China during the last 100 years, Chinese J. Atmos. Sci., 30, 464–474, 2006 (in Chinese).

Mann, H. B.: Nonparametric Tests against Trend, Econometrica, 13, 245–259, 1945.

Mantua, N. J. and Hare, S. R.: The Pacific decadal oscillation, J. Oceanogr., 58, 35–44, 2002.

Meehl, G. A., Arblaster, J. M., and Collins, W. D.: Effects of black carbon aerosols on the Indian monsoon, J. Climate, 21, 2869–2882, doi:10.1175/2007jcli1777.1, 2008.

Mitchell, T. D. and Jones, P. D.: An improved method of constructing a database of monthly climate observations and associated high-resolution grids, Int. J. Climatol., 25, 693–712, doi:10.1002/Joc.1181, 2005.

Ninomiya, K. and Kobayashi, C.: Precipitation and moisture balance of the Asian summer monsoon in 1991 Part II: Moisture transport and moisture balance, J. Meteorol. Soc. Jpn, 77, 77–99, 1999.

Otterå, O. H.: Simulating the effects of the 1991 Mount Pinatubo volcanic eruption using the ARPEGE atmosphere general circulation model, Adv. Atmos. Sci., 25, 213–226, doi:10.1007/s00376-008-0213-3, 2008.

Otterå, O. H., Bentsen, M., Bethke, I., and Kvamstø, N. G.: Simulated pre-industrial climate in Bergen Climate Model (version 2): model description and large-scale circulation features, Geosci. Model Dev., 2, 197–212, doi:10.5194/gmd-2-197-2009, 2009.

Otterå, O. H., Bentsen, M., Drange, H., and Suo, L. L.: External forcing as a metronome for Atlantic multidecadal variability, Nat. Geosci., 3, 688–694, doi:10.1038/Ngeo955, 2010.

Piao, S. L., Ciais, P., Huang, Y., Shen, Z. H., Peng, S. S., Li, J. S., Zhou, L. P., Liu, H. Y., Ma, Y. C., Ding, Y. H., Friedlingstein, P., Liu, C. Z., Tan, K., Yu, Y. Q., Zhang, T. Y., and Fang, J. Y.: The impacts of climate change on water resources and agriculture in China, Nature, 467, 43–51, doi:10.1038/Nature09364, 2010.

Qu, X. and Huang, G.: Impacts of tropical Indian Ocean SST on the meridional displacement of East Asian jet in boreal summer, Int. J. Climatol., 32, 2073–2080, 2012

Rayner, N. A., Parker, D. E., Horton, E. B., Folland, C. K., Alexander, L. V., Rowell, D. P., Kent, E. C., and Kaplan, A.: Global analyses of sea surface temperature, sea ice, and night marine air temperature since the late nineteenth century, J. Geophys. Res.-Atmos., 108, 4407, doi:10.1029/2002jd002670, 2003.

Salas-Melia, D.: A global coupled sea ice-ocean model, Ocean Model., 4, 137–172, 2002.

Shen, C. M., Wang, W. C., Hao, Z. X., and Gong, W.: Characteristics of anomalous precipitation events over eastern China during the past five centuries, Clim. Dynam., 31, 463–476, doi:10.1007/s00382-007-0323-0, 2008.

Smith, T. M., Reynolds, R. W., Peterson, T. C., and Lawrimore, J.: Improvements to NOAA's historical merged land-ocean surface temperature analysis (1880–2006), J. Climate, 21, 2283–2296, doi:10.1175/2007jcli2100.1, 2008.

Tanre, D., Geleyn, J., and Slingo, J.: First results of the introduction of an advanced aerosol-radiation interaction in the ECMWF low resolution global model, in: Aerosols and their climatic effects, edited by: Gerber, H. E. and Deepak, A., A. Deepak Publ., Hampton, Virginia, USA, 133–177, 1984.

Tao, S. Y. and Chen, L.: A review of recent research on the East Asian summer monsoon in China, in: Monsoon Meteorology, edited by: Chang, C. P. and Krishnamurti, T. N., 7, Oxford University Press, 60–92, 1987.

Tao, S. Y. and Zhu, K. F.: The variation of 100mb circulation over South Asia in summer and its association with march and withdraw of west Pacific subtropical high, Acta Meteorol. Sin., 34, 385–395, 1964.

Terray, L. and Thual, O.: Oasis: le couplage océan-atmosphére, La Météorologie, 10, 50–61, 1995.

Terray, L., Thual, O., Belamari, S., Deque, M., Dandin, P., Delecluse, P., and Levy, C.: Climatology and Interannual Variability Simulated by the Arpege-Opa Coupled Model, Clim. Dynam., 11, 487–505, 1995.

Trenberth, K. E. and Dai, A.: Effects of Mount Pinatubo volcanic eruption on the hydrological cycle as an analog of geoengineering, Geophys. Res. Lett., 34, L15702, doi:10.1029/2007gl030524, 2007.

Uppala, S. M., Kallberg, P. W., Simmons, A. J., Andrae, U., Bechtold, V. D., Fiorino, M., Gibson, J. K., Haseler, J., Hernandez, A., Kelly, G. A., Li, X., Onogi, K., Saarinen, S., Sokka, N., Allan, R. P., Andersson, E., Arpe, K., Balmaseda, M. A., Beljaars, A. C. M., Van De Berg, L., Bidlot, J., Bormann, N., Caires, S., Chevallier, F., Dethof, A., Dragosavac, M., Fisher, M., Fuentes, M., Hagemann, S., Holm, E., Hoskins, B. J., Isaksen, L., Janssen, P. A. E. M., Jenne, R., McNally, A. P., Mahfouf, J. F., Morcrette, J. J., Rayner, N. A., Saunders, R. W., Simon, P., Sterl, A., Trenberth, K. E., Untch, A., Vasiljevic, D., Viterbo, P., and Woollen, J.: The ERA-40 re-analysis, Q. J. Roy. Meteor. Soc., 131, 2961–3012, doi:10.1256/Qj.04.176, 2005.

Wang, H., Sun, J., and Fan, K.: Relationships between the North Pacific Oscillation and the typhoon/hurricane frequencies, Sci. China Ser. D, 50, 1409–1416, 2007.

Wang, H. J.: The weakening of the Asian monsoon circulation after the end of 1970's, Adv. Atmos. Sci., 18, 376–386, 2001.

Wang, H. J.: The instability of the East Asian summer monsoon-ENSO relations, Adv. Atmos. Sci., 19, 1–11, 2002.

Wang, T. and Wang, H. J.: Mid-Holocene Asian summer climate and its responses to cold ocean surface simulated in the PMIP2 OAGCMs experiments, J. Geophys. Res.-Atmos., 118, 4117–4128, doi:10.1002/jgrd.50287, 2013.

Wang, T., Ottera, O. H., Gao, Y. Q., and Wang, H. J.: The response of the North Pacific Decadal Variability to strong tropical volcanic eruptions, Clim. Dynam., 39, 2917–2936, doi:10.1007/s00382-012-1373-5, 2012.

Wang, T. J., Li, S., Shen, Y., Deng, J. J., and Xie, M.: Investigations on direct and indirect effect of nitrate on temperature and precipitation in China using a regional climate chemistry modeling system, J. Geophys. Res.-Atmos., 115, D00K26, doi:10.1029/2009jd013264, 2010.

Wang, Y. and Yan, Z. W.: Changes of frequency of summer precipitation extremes over the Yangtze River in association with large-scale oceanic-atmospheric conditions, Adv. Atmos. Sci., 28, 1118–1128, 2011.

Webster, P. J.: The elementary monsoon, Monsoons, edited by: Fein, J. S. and Stephens, P. L., Wiley Interscience, New York, 3–32, 1987.

Wu, R. G., Kinter, J. L., and Kirtman, B. P.: Discrepancy of interdecadal changes in the Asian region among the NCEP-NCAR reanalysis, objective analyses, and observations, J. Climate, 18, 3048–3067, 2005.

Xie, S. P., Hu, K. M., Hafner, J., Tokinaga, H., Du, Y., Huang, G., and Sampe, T.: Indian Ocean Capacitor Effect on Indo-Western Pacific Climate during the Summer following El Nino, J. Climate, 22, 730–747, 2009.

Zhai, P. M., Zhang, X. B., Wan, H., and Pan, X. H.: Trends in total precipitation and frequency of daily precipitation extremes over China, J. Climate, 18, 1096–1108, doi:10.1175/Jcli-3318.1, 2005.

Zhao, P., Zhang, X., Li, Y., and Chen, J.: Remotely modulated tropical-North Pacific ocean-atmosphere interactions by the South Asian high, Atmos. Res., 94, 45–60, 2009.

Zhao, P., Yang, S., and Yu, R. C.: Long-Term Changes in Rainfall over Eastern China and Large-Scale Atmospheric Circulation Associated with Recent Global Warming, J. Climate, 23, 1544–1562, doi:10.1175/2009jcli2660.1, 2010.

Zhou, T. J. and Yu, Y. C.: Atmospheric water vapor transport associated with typical anomalous summer rainfall patterns in China, J. Geophys. Res.-Atmos., 110, D08104, doi:10.1029/2004JD005413, 2005.

Zhou, T. J., Yu, R. C., Zhang, J., Drange, H., Cassou, C., Deser, C., Hodson, D. L. R., Sanchez-Gomez, E., Li, J., Keenlyside, N., Xin, X. G., and Okumura, Y.: Why the Western Pacific Subtropical High Has Extended Westward since the Late 1970s, J. Climate, 22, 2199–2215, doi:10.1175/2008jcli2527.1, 2009.

Zhu, Y. L., Wang, H. J., Zhou, W., and Ma, J. H.: Recent changes in the summer precipitation pattern in East China and the background circulation, Clim. Dynam., 36, 1463–1473, doi:10.1007/s00382-010-0852-9, 2011.

Zuo, Z. Y., Yang, S., Kumar, A., Zhang, R. H., Xue, Y., and Jha, B.: Role of Thermal Condition over Asia in the Weakening Asian Summer Monsoon under Global Warming Background, J. Climate, 25, 3431–3436, doi:10.1175/Jcli-D-11-00742.1, 2012.